A&A 432, 547–557 (2005)
DOI: 10.1051/0004-6361:20041891

Astronomy & Astrophysics

The 90–110 μm dust feature in low to intermediate mass protostars: Calcite?⋆

A. Chiavassa[1], C. Ceccarelli[1], A. G. G. M. Tielens[2], E. Caux[3], and S. Maret[1]

[1] Laboratoire d'Astrophysique, Observatoire de Grenoble, BP 53, 38041 Grenoble Cedex 09, France
e-mail: cecilia.ceccarelli@obs.ujf-grenoble.fr
[2] Kapteyn Astronomical Instute, BO Box 800, 9700 AV Groningen, The Netherlands
[3] CESR CNRS - UPS, BP 4346, 31028, Toulouse Cedex 04, France

Received 24 August 2004 / Accepted 25 October 2004

Abstract. We present ISO spectra between 60 and 180 μm of 32 protostars of low to intermediate mass. About half of the spectra present a dust feature between ~90 and ~110 μm. We describe the observational characteristics of this feature, which seems to be due to one single carrier. In Class 0 sources the feature peaks around 100 μm, while in AeBe stars it peaks around 95 μm. The feature peak position seems to mostly depend on the temperature of the dust of the source, suggesting reprocessing of the dust. We present arguments for the identification of the observed feature as due to calcite, and estimate that about 10% to 30% of elemental Ca is locked up in it. Therefore, calcite seems to be formed relatively easily around protostars despite the observation that on Earth it needs aqueous solutions. This rises the question of whether conditions simulating liquid water are common around forming stars and what creates them.

Key words. ISM: abundances – ISM: molecules – stars: formation – ISM: dust, extinction – ISM: lines and bands – infrared: ISM

1. Introduction

Infrared spectroscopy provides a crucial tool for identifying the dust composition around protostars. Historically, the Near to Mid InfraRed (NIR and MIR respectively) has been the frequency range of choice for such studies as many features of dust cores and icy mantles lie in that range. Over the years, an impressive amount of work has accumulated and has provided a detailed view of the dust mineralogy in many objects. For protostars, the emphasis has been on relatively evolved systems emitting strongly in the NIR and MIR (needed to observe the features). Much less has been done on the embedded and presumably younger low mass protostars because they are faint in the NIR/MIR.

Since the Far InfraRed (FIR) range is much less rich in features (e.g. Draine 2003) and more difficult to observe, it has received much less attention than the NIR/MIR for mineralogy studies. Yet, some important minerals have distinctive features in the FIR. One notable example is the case of carbonates (e.g. Farmer 1970). Because of telluric absorption, FIR spectroscopic observations are impossible with ground telescopes and have become routine only fairly recently with the *Long Wavelength Spectrometer* (LWS; Clegg et al. 1996) on board the *Infrared Space Observatory* (ISO, Kessler et al. 1996). Hence, the first studies of the FIR-based mineralogy of interstellar dust have only appeared in the last few years. Waters & Waelkens (1998), Barlow et al. (1998) and Malfait et al. (1999) reported the presence of a broad feature around 100 μm in some young and evolved stars. Malfait et al. (1999) attributed this feature to the hydrous silicate, montmorillonite (Koike et al. 1990). Subsequently, Kemper et al. (2002a,b) discovered a feature at 92 μm in the spectrum of the planetary nebula, NGC 6302, which they assigned to calcite. A similar feature was discovered in the spectrum of the protostar, NGC 1333–IRS 4 and also assigned to calcite (Ceccarelli et al. 2002; hereinafter Paper I). Later, a similar feature was detected in two other star forming regions, and attributed to carbon onions (Onaka & Okada 2003).

The discovery of calcite is not just a new beast in the zoo of interstellar minerals; it also points towards a formation mechanism which does not involve liquid water. On large Solar System bodies like the Earth, carbonates form through the weathering of silicates in a watery (CO_3^{2-}) solution. Likewise, the presence of carbonates in interplanetary dust particles (IDPs) and asteroids (meteorites) is attributed to aqueous alteration on a large parent body which was shattered into smaller pieces (Richardson 1978; Macdougall et al. 1984). Indeed, carbonates have also been discovered in Martian

⋆ Based on observations with ISO, an ESA project with instruments funded by ESA Member States (especially the PI countries: France, Germany, The Netherlands and the United Kingdom) with the participation of ISAS and NASA.

meteorites (Gooding et al. 1988, 1991; Treiman et al. 1993) and considered as further evidence for liquid water on Mars (Wentworth & Gooding 1994; Bridges et al. 2001). Hence, the discovery of carbonates in sources outside the Solar System represents a new frontier in carbonate formation theories, since no liquid water is present in these objects, and other efficient formation mechanisms seem implied (Kemper et al. 2002a).

In this article we analyze and interpret far-IR observations of a sample of low to intermediate mass protostars. The article is organized as follows: in Sect. 2 we present the observational framework, namely the selected sample of sources, their LWS spectra and the excess between 90 and 110 μm visible in several of them. In Sect. 3 we discuss the characteristics of the detected excess and present arguments for its identification as due to calcite. Section 4 summarizes the article and discusses some prospectives on future work.

2. The observational framework

2.1. Selected sample

The sample consists of several low to intermediate mass protostars, whose LWS spectrum has been previously published in the literature. In total, there are 32 sources, of which 2/3 are low mass and the rest intermediate mass protostars. The sample is presented in Table 1, which also gives their distance, luminosity and source class. The largest group is represented by the group of Class 0 sources (15 sources), followed by the group of AeBe sources (11), which includes, however, embedded to visible intermediate mass sources. We also included 3 Class I sources and 3 T Tau stars.

Evidently, the resulting sample is by no means representative of all low to intermediate mass protostars. Likely, the Class 0 sub-sample can be considered reasonably representative of this class of sources, for it includes practically all the brightest Class 0 sources known so far (e.g. André et al. 2000) and in the following we will discuss this sub-sample in more detail, when appropriate.

2.2. LWS data reduction

The LWS data of the sample sources were taken from the ISO Data Archive (IDA), at `www.iso.vilspa.esa.es/ida/`, which contains the V10 version data, namely the final LWS data products. We reduced all the spectra using the last version of the ISAP software package. In the LWS, each detector scans a small wavelength range (cf., Fig. 1). The resulting spectra show small jumps in flux level between these individual detector ranges. In principle, such jumps may reflect dark current variations during the observations and/or absolute flux calibration uncertainties. The former would give rise to spurious additive offsets while the latter result in multiplicative offsets. For these weak souces, dark current errors are expected to dominate and, hence, we have stitched the individual detectors in each spectrum together by adding an offset. We have explicitly checked that the adopted method does not introduce artificial features in the resulting spectrum. Fortunately, as Fig. 1 illustrates, the relevant wavelength range (90–110 μm) is in its entirety contained within the LW1 detector and, in addition, two detectors, SW5 and LW2, overlap over a large fraction of the LW1 range. Furthermore, we carefully checked that the spectrum at those wavelengths is not affected by the choice of the reference detector to which the rest of the spectrum is stitched. The left panel of Fig. 1 illustrates the effect of the choice of the reference detector for the source L1551-IRS5, the source for which this choice had the largest effect on the resulting spectrum. In one reduction the reference detector is LW4, while in the second it is SW3 (these are the two detectors that were used as reference in the stitching procedure). The right panel of the figure shows that while the different choice changes the absolute flux (by about a factor 2), the shape of the spectrum in the 90–110 μm range is practically unaffected (the influence on the excess is further discussed in Sect. 2.4 and shown in Fig. 4).

2.3. Continuum removal

In order to detect the presence of the dust feature in the 90–110 μm range, the continuum has been removed. Several authors have remarked that the FIR ($\lambda \geq 60$ μm) to millimeter continuum spectrum of embedded protostars can be reasonably well described by a single blackbody multiplied by the dust opacity k_λ, which in these wavelength ranges is typically approximated by a power law $k_\lambda = k_0(\lambda_0/\lambda)^\beta$ (e.g. Henning et al. 1995). The value of β depends on the dust composition, shape and size (coagulation of the mantle formation), and it varies between 1 and 2 in Class 0 sources (e.g. Ossenkopf & Henning 1994; Chandler & Richer 2000). In the following we will refer to this as a "modified blackbody", for brevity.

Given the relatively large LWS beam (~80″), the signal includes emission from the protostar as well as from the parental cloud. We therefore modeled the emission with at least two modified-blackbodies, in order to account for the cold dust in the cloud. A third component was sometimes required to account for the warmer dust originating in the innermost regions of the envelopes. Therefore, following the analysis in Paper I, we modeled the source spectra with a "three modified-blackbodies" emission model, as follows:

$$I_\lambda = \sum_i BB(\lambda, T_i) \cdot \left[1 - \exp[\tau_i(60\mu\mathrm{m}) \cdot (60/\lambda_{\mu\mathrm{m}})^{\beta_i}\right] \cdot \Omega_i \qquad (1)$$

which is the sum of three $BB(\lambda, T_i)$ at the temperature T_i and wavelength λ. The free parameters are the opacity τ_i for each modified blackbody, the power β_i, the temperature T_i and the solid angle Ω_i of the warm and hot component (the cold component is always assumed to fill the LWS beam). For each source we found the best fit to the data, by minimizing the χ^2, defined as the sum of the squares of the differences of the theoretical and observed values, normalized to the number of points. In addition, the fit to the continuum is not allowed to overestimate the observed flux, and the 90–110 μm wavelength range is excluded, together with the ranges where gas lines are present (see for example Fig. 2 caption).

The 3-modified-blackbodies method gives rather satisfying results for most of the sources. Two typical examples, EL29 and L1448-mm, are shown in Fig. 2. As for IRAS 4 (Paper I),

Table 1. List of the sources considered in this study. The third, fourth and fifth columns report the bolometric luminosity, distance, and class of each source. The sixth and seventh columns give the temperature and opacity of the warm dust component which best fits the continuum (see text for details). The average errors are 1 K and 0.1 respectively. The next three columns report the parameters of the best fit of the 90–110 μm excess with a Gaussian: the wavelength $\lambda_{\rm fea}$ at which the feature peaks, the width of the feature $\sigma_{\rm fea}$, and the amplitude of the excess $A_{\rm fea}$. The average errors on $\lambda_{\rm fea}$ and $\sigma_{\rm fea}$ are 1 and few μm respectively, as discussed in the text. The statistical errors on the Gaussian amplitude $A_{\rm fea}$ are of the order of 10%. However, the uncertainty on $A_{\rm fea}$ is dominated by the removal of the dust continuum, which is difficult to quantify, but which can be up to 50% (see text). The last three columns report the mass of calcite required to reproduce the feature and the ratio of calcite to warm dust mass, and the reference of the published LWS spectra, according to the footnote 1. * Sources where the fit is difficult and the results ambiguous. References: 1- Giannini et al. (1999), A&A, 346, 617; 2- Spinoglio et al. (2000), A&A, 353, 1055; 3- Nisini et al. (1999), A&A, 350, 529; 4- Nisini et al. (2000), A&A, 360, 297; 5- Nisini et al. (1999), A&A, 343, 266; 6- Ceccarelli et al. (1998), A&A, 331, 372; 7- Benedettini et al. (2000), A&A, 359, 148; 8- Molinari et al. (2000), ApJ, 538, 698; 9- Ceccarelli et al. (2002), A&A, 395, 863; 10- Caux et al. (1999), The Universe as Seen by ISO, ed. P. Cox, & M. F. Kessler, ESA-SP 427, 643; 11- Maret et al. (2002), A&A, 395, 573; 12- Giannini et al. (2001), ApJ, 555, 40; 13- Nisini et al. (2002), ApJ, 574, 246; 14- Larsson et al. (2002), A&A, 386, 1055; 15- White et al. (2000), A&A, 364, 741; 16- Lorenzetti et al. (2000), A&A, 357, 1035; 17- Lorenzetti et al. (1999), A&A, 346, 604; 18; Creech-Eakman et al. (2002), A&A, 385, 546.

Nr.	Name	$L_{\rm bol}$ ($L_\odot$)	Dist (pc)	Class	$T_{\rm Warm}$ (K)	$\tau_{\rm Warm}$	$\lambda_{\rm fea}$ (μm)	$\sigma_{\rm fea}$ (μm)	$A_{\rm fea}$ (erg cm^{-2}s$^{-1}\mu$m^{-1})	$M_{\rm Calcite}$ ($M_\oplus$)	Ratio (%)	Ref.
1	L1448-mm	11	300	Class 0	30	2.2	101	13	0.3	2.0	0.3	3
2	L1448-IRS3	9	300	Class 0	21	5.1	105	12	0.2	3.5	0.2	4
3	B335	3	250	Class 0	25	1.1	...	...	≤0.05	...	...	5
4	I16293	13	120	Class 0	47	0.01	96	9	1.2	0.2	0.2	6
5	HH25-mms	6	450	Class 0	30	1.5	100	13	0.2	3.1	0.4	7
6	NGC 1333-I2	16	220	Class 0	45	0.5	...	...	≤0.2	...	...	10
7	NGC 1333-I4	11	220	Class 0	25	1.5	98	11	0.3	3.0	0.4	11
8	HH211-mm	5	300	Class 0	24	1.4	99	27	0.4	4.0	0.9	12
9	L1641-VLA1	50	450	Class 0	35	1.2	100	9	0.2	0.1	0.07	12
10	L1527-mm	2	140	Class 0	32	1.0	103	10	0.2	0.1	0.4	12
11	HH24-mms	5	450	Class 0	31	0.8	103	10	0.3	0.1	1	7
12	L723-mm	3	300	Class 0	20	1.2	...	...	≤0.03	...	...	12
13	L1157-mm	11	440	Class 0	26	1.4	...	...	≤0.04	...	...	12
14	Ser-SMM3	2–30	310	Class 0	29	2.0	...	...	≤0.2	...	...	14
15	Ser-SMM4	3–30	310	Class 0	32	1.3	100	16	0.5	2.0	0.8	14
16	SVS13	31	220	Class I	48	0.7	...	...	≤0.2	...	...	8
17	WL16(YLW5)	12	120	Class I	45	0.2	94	21	0.8	0.15	2	13
18	L1551-IRS5	30	160	Class I	50	0.9	105	11	0.4	0.15	0.2	15
19	T Tau	12	160	T Tau	47	0.8	...	...	≤0.16	...	...	2
20	V1331Cyg*	36	600	T Tau	32	0.9	...	...	...	...	...	16
21	AA Tau	0.8	140	T Tau	26	3.6	...	...	≤0.04	...	...	18
22	EL29	23	120	AeBe	46	1.0	96	16	0.8	0.15	0.05	9
23	RCrA-IRS7	99	130	AeBe	51	1.1	92	6	1.5	0.1	0.7	1
24	LkHα234	283	1000	AeBe	42	2.3	...	...	...	...	...	1
25	LkHα198	340	600	AeBe	47	0.5	91	8	0.4	1.2	0.2	17
26	V376Cas*	517	600	AeBe	53	0.7	...	...	≤0.8	...	...	17
27	HD97048*	30	150	AeBe	41	1.8	...	...	...	...	...	17
28	AB Aur	48	144	AeBe	51	0.3	...	...	≤0.09	...	...	18
29	CQ Tau	5	100	AeBe	45	0.1	96	13	0.1	0.01	0.5	18
30	HD36112	22	200	AeBe	41	0.5	...	...	≤0.03	...	...	18
31	LkHα233	200	880	AeBe	46	0.6	95	13	0.3	0.2	6	18
32	MWC480	–	131	AeBe	44	0.4	...	...	≤0.04	...	...	18

the model continuum fits the observations to within a few percent over most of the spectrum, except for the 90–110 μm region, where no choice of the parameters can reproduce the excess.

We verified that the simplified 3-modified-blackbodies analysis of the spectrum is reliable to extract the 90–110 μm excess, by comparing our 3-modified-blackbodies procedure with more sophisticated models of the dust continuum. To do that, we cross-checked our results with the radiative transfer code DUSTY (Ivezić et al. 1999), publicly available at `http://www.pa.uky.edu/~moshe/dusty`. We have computed the spectral energy distributions (SED) of some sources in common with the sample studied in detail by Joergensen et al. (2002). In this analysis, we have taken the parameters derived by those authors from their analysis of the SED and emission maps at 800 and 450 μm. The agreement between the DUSTY predictions (using the Joergensen et al. parameters) and the LWS data is not as good as our simplified analysis. This is perhaps not surprising as these models are not specifically optimized to fit the LWS data. Nevertheless, this test clearly

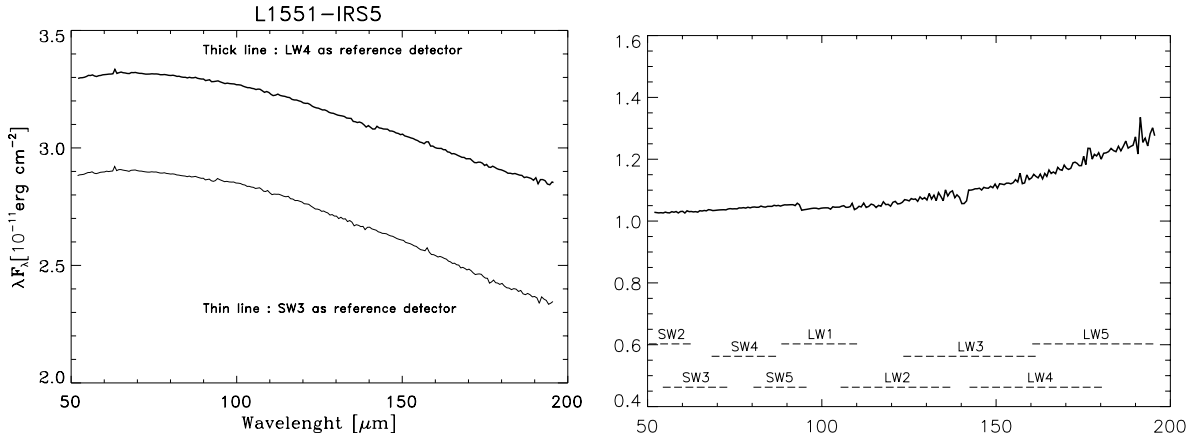

Fig. 1. Example of the spectrum of L1551-IRS5. The left panel shows the reduced spectrum obtained by using two different reference detectors: LW4 (thick line) and SW3 (thin line) respectively. The right panel shows the ratio between the two spectra (obtained with LW4 and SW3 as reference detectors), as well as the range of each LWS detector. In the relevant wavelength range (85–110 μm), the spectrum obtained by taking SW3 as reference detector has a small jump at about 95 μm, which is also visible in the ratio of the right panel, and in the plot of the 90–110 μm excess shown in Fig. 4.

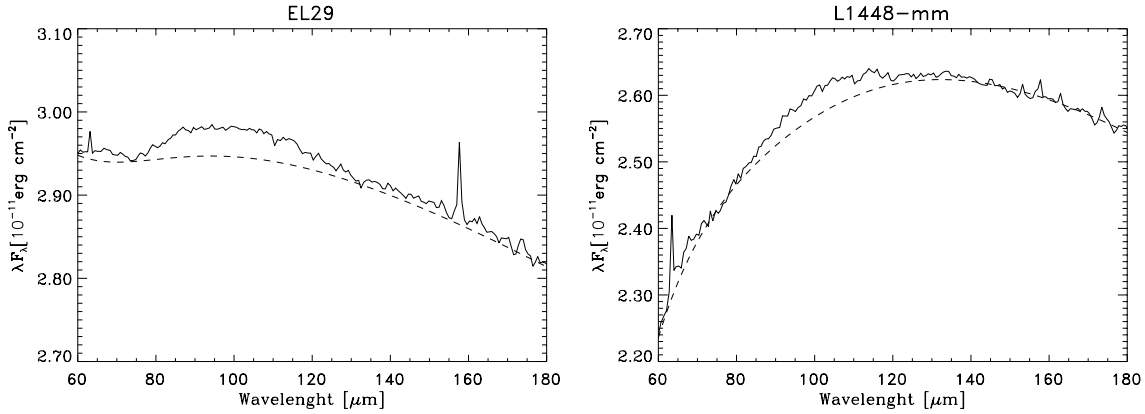

Fig. 2. Example of the spectra of EL29 (*left panel*) and L1448-mm (*right panel*): the dashed lines represent the best fit obtained with the 3-modified-blackbodies method described in the text. While EL29 is a typical example of a relatively warm source, L1448-mm is a typical example of a relatively cold source (see Table 1). Note that the spikes in the spectra are lines and not noise: the OI-63 μm and CII-158 μm lines are particularly evident in both spectra.

confirms that our simplified 3-modified-blackbodies analysis does a good job in describing the continuum, and, mostly important, does not miss any 90–110 μm emission with respect to complex radiative transfer models, and, in this respect, is fully reliable. As a published example of a sophisticated analysis of LWS continuum spectra, the reader can examine Boogert et al. (2002), who fit the LWS spectrum of EL29 with a flared disk model. Indeed, in retrospect, the 90–110 μm excess is evident in that spectrum.

Finally, a few sources have LWS spectra difficult to fully reproduce with the 3-modified-blackbodies method. Usually, the region at $\lambda \leq 70$ μm presents a difficulty, as shown in the example of Fig. 3. In the following we will explicitly mention the sources where the fit is somewhat problematic.

2.4. The excess at 90–110 μm

After removal of the continuum, about half of the sources show an excess in the 90–110 μm wavelength range. We found that in some cases the amplitude of the excess (i.e. the flux above the continuum subtracted spectrum) depends on the reference detector chosen in the data reduction. However, we emphasize that also in those cases the presence of the excess is robust. As mentioned in in Sect. 2.3, the worst case is presented by L1551-IRS5 (Fig. 1). Figure 4 shows the excess obtained by using two different reference detectors, LW4 and SW3 respectively for L1551-IRS5. The amplitude of the excess is about a factor of two lower when LW4 is chosen, but the excess is still clearly present. Hence, conservatively, we will assume that the overall continuum removal procedure gives rise to about 50% uncertainty in the quoted amplitudes. In addition, the continuum removal can also affect the peak position and width of the feature. Typically, we found that this uncertainty is around 1 μm and few μm, respectively. Note also the right panel of Fig. 4, where we again show the coverage of the SW5, LW1 and LW2 detectors in the 85–110 μm range. Because three detectors overlap the wavelength range of the feature, its detection is a robust non-instrumental result. Finally, we checked that there is no evidence for a dependency of the presence and/or amplitude of the excess on the source flux, again ruling against an instrumental effect.

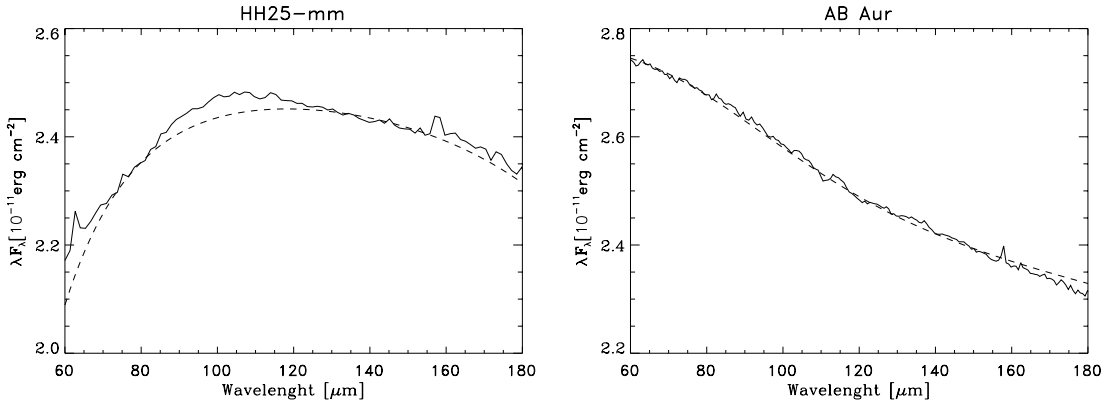

Fig. 3. The *left panel* shows an example of a source spectrum difficult to fit: HH25-mm. The dashed line represents the best fit obtained with the 3-modified-blackbodies method described in the text. The fit is poor at $\lambda \leq 80$ μm. *The right panel* shows a spectrum with no excess in the 90–110 μm range: AB Aur.

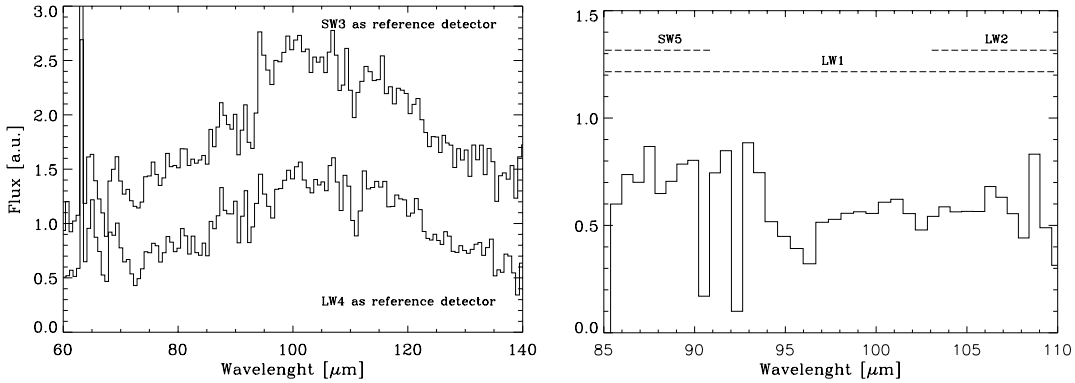

Fig. 4. The 90–110 μm excess in L1551-IRS5, derived using two different reference detectors (*left panel*): SW3 (upper curve) and LW4 (lower curve), as described in the text and shown in Fig. 1. The right panel presents the ratio of these two spectra as well as the range of the SW5, LW1 and LW2 detectors.

Figure 5 shows the 90–110 μm excess in all sources where the excess was found. Perusal of the spectra displayed in Fig. 5 shows that the characteristics of the feature vary from source to souce. In particular, we recognize a broad feature peaking at ∼105 μm in L1551-IRS5. Several of the Class 0 sources show an emission feature which is very similar in peak position and width. However, in for example NGC 1333-IRAS 4, the peak shifts to shorter wavelengths and the feature is narrower. This difference is even more pronounced when examining the Herbig AeBe spectra. For example, in LKHα233, the feature peaks at even shorter wavelengths than NGC 1333-IRAS 4 but is also somewhat broader.

To summarize, the peak of the feature shifts from source to source. In some sources, it peaks around 95 μm (sources near the top of the figure), whereas in other sources it has shifted to around 105 μm (sources near the bottom of the figure). We tried to understand whether this results from blending of two features in different proportions from source to source, or whether this is indeed one feature whose peak and shape vary from source to source. For this, we first fitted the excess with a single Gaussian function and then with a combination of two Gaussians. The parameters of the single Gaussian which best fit the data are listed in Table 1: the position of the peak $\lambda_{\rm fea}$, the width of the Gaussian $\sigma_{\rm fea}$, and the amplitude of the Gaussian $A_{\rm fea}$ (i.e. the feature strength). We also carried out a fit with two Gaussian functions, as follows. The first Gaussian has the peak and width fixed and set equal to the single Gaussian that best fits the excess of LkHα198 (the source with the cleanest 95 μm fit). In essence, we assume that the feature in the LkHα198 spectrum, which is the closest to the shape of the calcite feature (see Sect. 3.3), is one of the two presumed dust components. The amplitude of this first Gaussian is left as a free parameter of the fit, together with the peak, width, and amplitude of the second Gaussian function. Figure 6 presents the fits with the two Gaussian functions for three typical cases. Except for EL29, the observed feature in each source seems dominated by a single component. This behavior suggests that the feature is due to one carrier only, but that its detailed characteristics – namely its peak position and width – are sensitive to the local physical conditions and/or history of the source. This will be discussed further below.

3. Discussion

3.1. Detection statistics and feature characteristics

The 90–110 μm excess emission has been detected in 17 out of 32 sources, suggesting that it is a rather common propriety of protostars. Around 67% of Class 0 protostars and 45% of

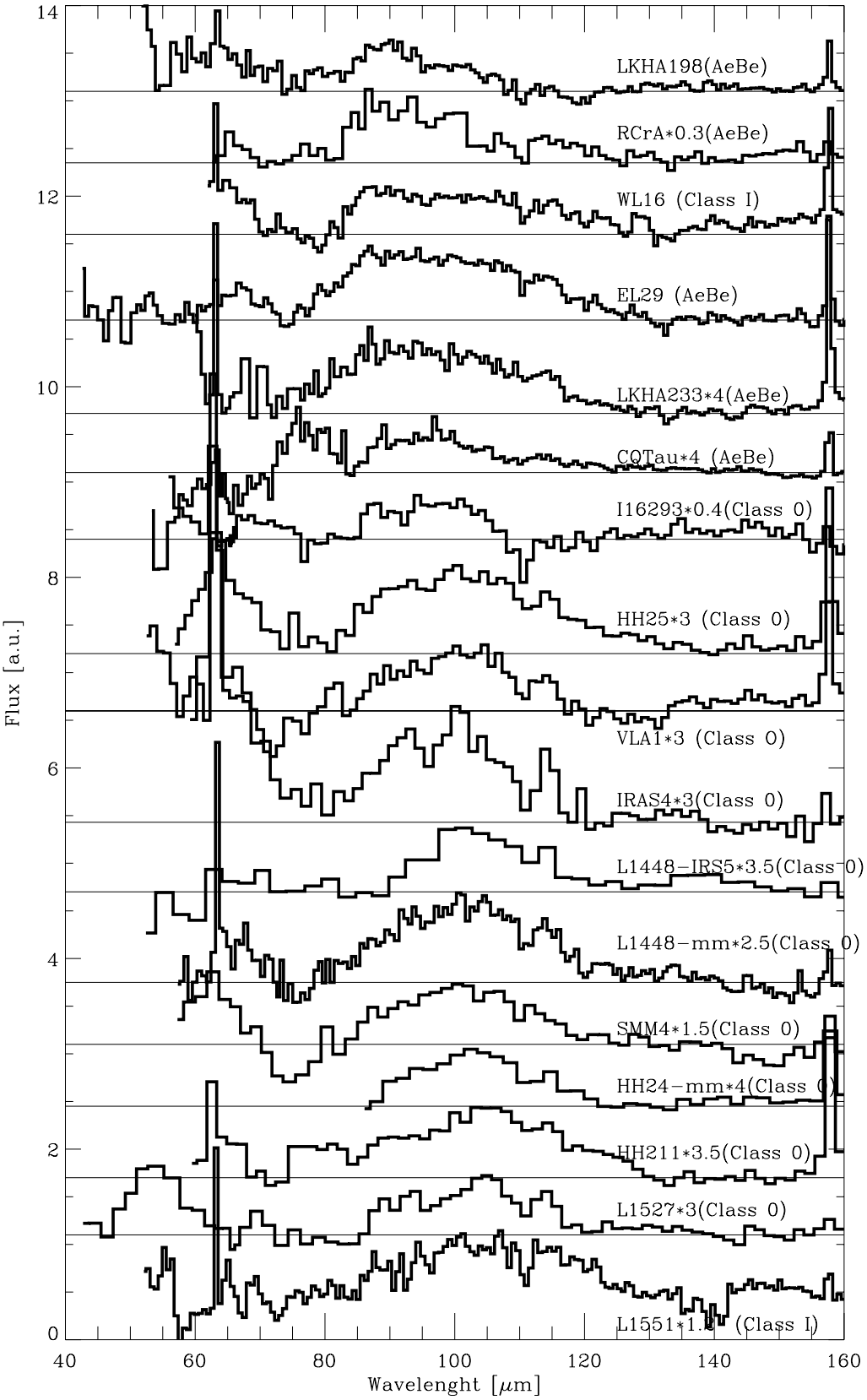

Fig. 5. The excess of the continuum in the 90–110 μm wavelength range detected in 17 sources. Note that the spectra also show very clearly some bright gas lines: the OI-63 μm line, the CO 23-22 transition merged with the H_2O $4_{14}-3_{03}$ transition, resulting in a line at 114 μm, and, finally, the CII-158 μm. All sources are plotted on the same linear scale (in arbitrary units) but the spectra of some sources have been multiplied by a factor (indicated next to the source name) to enhance the visibility of the feature.

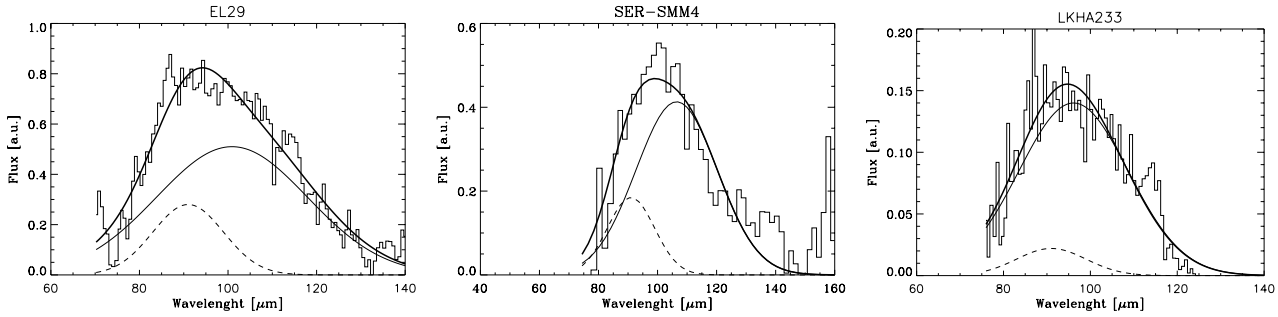

Fig. 6. Examples of the two Gaussians fit. The thick lines are the best fit obtained by adding two Gaussians: the thin lines show the contribution by the two Gaussians. EL29 (*left panel*) is the only source where the two Gaussians have almost a comparable amplitude. All other sources are similar to SER-SMM4 and LKHα233 (*middle and right panels* respectively), where one Gaussian totally dominates the fit.

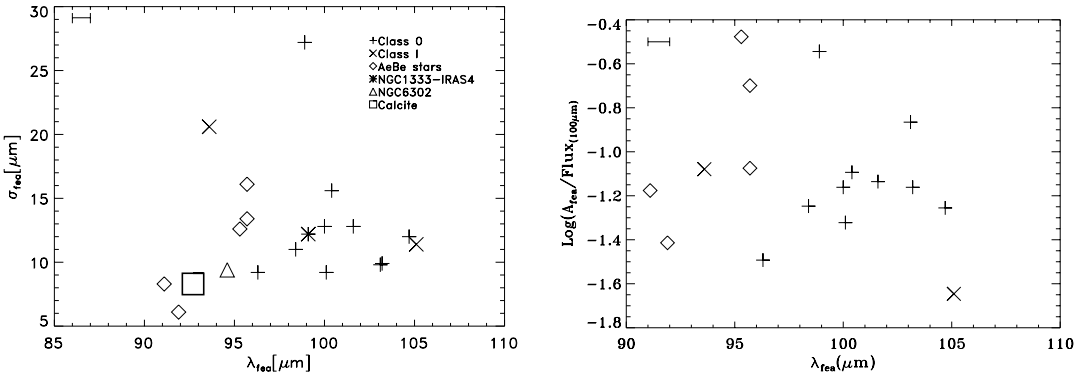

Fig. 7. The $\sigma_{\rm fea}$ and $A_{\rm fea}$ as function of $\lambda_{\rm fea}$ in the sources where the feature is detected (*left and right panels* respectively). Pluses mark Class 0 sources, crosses Class I sources, and diamonds AeBe sources. The triangle refers to NGC 6302 (Kemper et al. 2002b) and the star to NGC 1333-IRS4 (PaperI), where the feature has been first observed. The big square in the left panel indicates the position of the calcite, from laboratory measurements (Kemper et al. 2002b). The Class 0 sources with the largest $\sigma_{\rm fea}$ in the left panel is HH211-mm, which is a quite faint source and, hence, the derived parameters are rather uncertain. The bar in the top left corner of both plots shows the average error associated with the peak position wavelength.

Herbig AeBe stars present the excess. The characteristics of the feature depend on which of these two groups the source belongs to, as shown in Fig. 7. There is a clear dichotomy in the feature peak: in Class 0 sources the feature peaks at $\lambda \geq 96\,\mu$m, whereas, in Herbig AeBe sources, it peaks at shorter wavelengths. Unfortunately, the present statistics are not robust enough to say anything about Class I and T Tau sources. On the contrary, neither the width nor the strength of the feature seem to depend on the source class.

3.2. Correlations

Before discussing the possible origin/nature of the 90–110 μm feature, we will define the observational framework better, by examining various correlations between the feature parameters ($\lambda_{\rm fea}$, $\sigma_{\rm fea}$ and $A_{\rm fea}$, derived with the single Gaussian fit) and physical parameters associated with the sources. Figure 8 shows $\lambda_{\rm fea}$ as function of the $L_{\rm bol}$. This figure illustrates very graphically the striking difference in peak position between the groups of Class 0 and Herbig AeBe sources. At the same time, the absence of a correlation between the luminosity of the source and the peak position is also obvious.

Figures 9 and 10 show the three feature parameters as function of the cold and warm dust temperature respectively, as derived by the 3-modified-blackbodies procedure (Sect. 2.3).

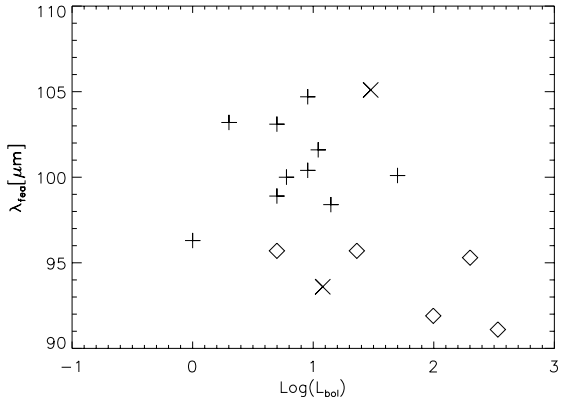

Fig. 8. $\lambda_{\rm fea}$ as function of the bolometric luminosity of the sources. The symbols are the same of Fig. 7.

There is no obvious relationship between the characteristics of the feature and the temperature of the cold dust. Very likely, this is because the warm dust dominates the emission where the feature emits. In contrast, when considering the warm component, the peak position shifts to longer wavelengths with decreasing dust temperature, possibly showing a correlation between the two quantities. This difference may reflect a dependence of the feature characteristics on the dust temperature

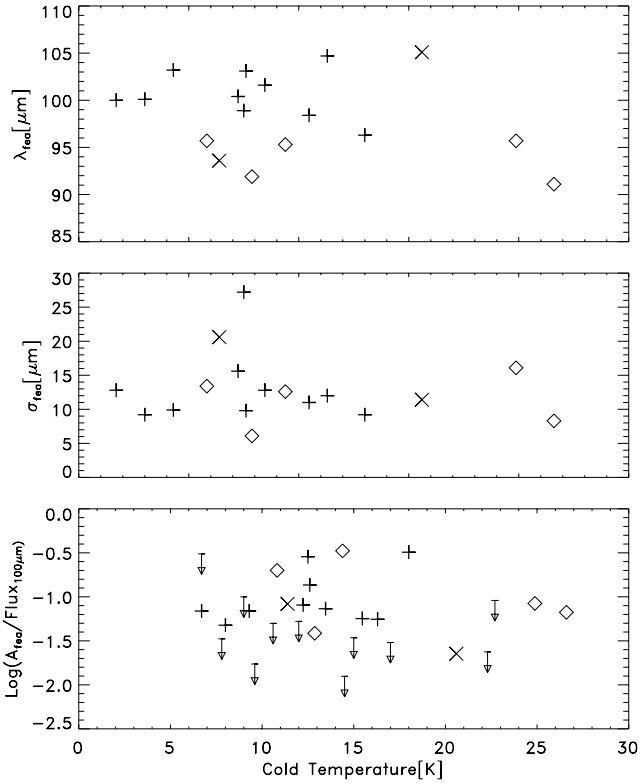

Fig. 9. The three parameters of the single Gaussian fit are plotted versus the cold temperature, as derived by the 3-modified-blackbodies procedure (see text for details). Symbols are as in Fig. 7. The arrows mark sources where only upper limits could be derived. No correlations with the cold dust temperature can be distinguished in these plots.

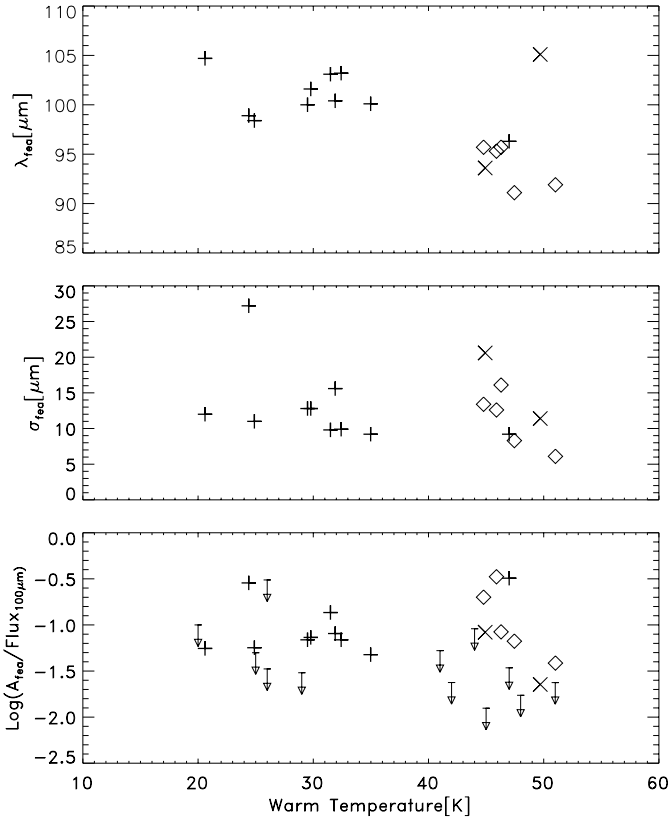

Fig. 10. The three parameters of the single Gaussian fit versus the warm temperature, as derived by the 3-modified-blackbodies procedure. Symbols are as in Fig. 7. The arrows mark sources where only upper limits could be derived. The Class 0 source which lies in the AeBe group space is HH211-mm. This analysis may suggest that this source, erroneously considered as Class 0 source, is indeed more evolved.

or a dependence of the dust characteristics on the type of source correlated to it, e.g. dust formation or previous history. Figure 11 displays the three parameters of the feature as function of the millimeter to bolometric luminosity ratio, in the subsample of Class 0 sources. There is no obvious dependence of the characteristics of the feature, included the peak position, on this parameter, which is often used to measure the evolutionary stage of the source (e.g. André et al. 2002). We therefore conclude that, at least within the Class 0 group, no evidence is found for dust feature reprocessing on the time scale of the Class 0 source age ($\sim 10^4$ yr). Finally, and disappointingly enough, these correlation studies do not present an obvious reason why half of the studied sources have this long wavelength feature and the other half of the sample does not.

3.3. Identification of the carrier: Calcite?

The 90–110 μm feature has been previously detected in a few other sources: the young disk source HD 142527 (Mafait et al. 1999), the planetary nebula NGC 6302 (Kemper et al. 2002a), NGC 1333-IRAS 4 (Paper I), and in the star forming regions, the Carina Nebula and Sharpless 171 (Onaka & Okada 2003). In the first three cases, it has been attributed to the hydrous silicate montmorillonite (Malfai et al.) and carbonate calcite (Kemper et al. 2002a,b and Paper I), which both require weathering for their formation. Alternatively, Onakada & Okada (2003) explored the possibility that this feature is due to carbon onions, i.e. graphite in curved shells. They found that the appearance of the feature is very sensitive to the assumed optical properties and to a fine tuning of the grain characteristics, which makes this possibility improbable in our opinion. We will hence not consider this hypothesis further.

On the contrary, in the following we explore the other two possibilities, namely that the 90–110 μm feature is due to either carbonate, calcite, or to the hydrous silicate, montmorillonite. In Fig. 7, the observed peak position and width of the 90–110 μm feature are compared to those of the calcite resonance feature as measured in the laboratory (Kemper et al. 2002b; see also the Jena-St.Petersburg Database of Optical Constants (`http://www.astro.spbu.ru/JPDOC/f-dbase.html`: Henning et al. 1999). The laboratory spectrum refers to a very pure sample of calcite ($CaCO_3$), with less than 0.1% of Si impurities. The peak of the feature of this crystal lies at 93 μm, and its width is about 8 μm, close to what we observe in our sample, especially with respect to the Herbig AeBe group. As noted before, the peak position of the feature shifts to longer wavelengths ($\sim$105 μm) in the Class 0 group, and appears also broader. This may reflect processing of the calcite mineral and/or a mineral with a different portion and/or different contributions of impurities. It is worth to note that

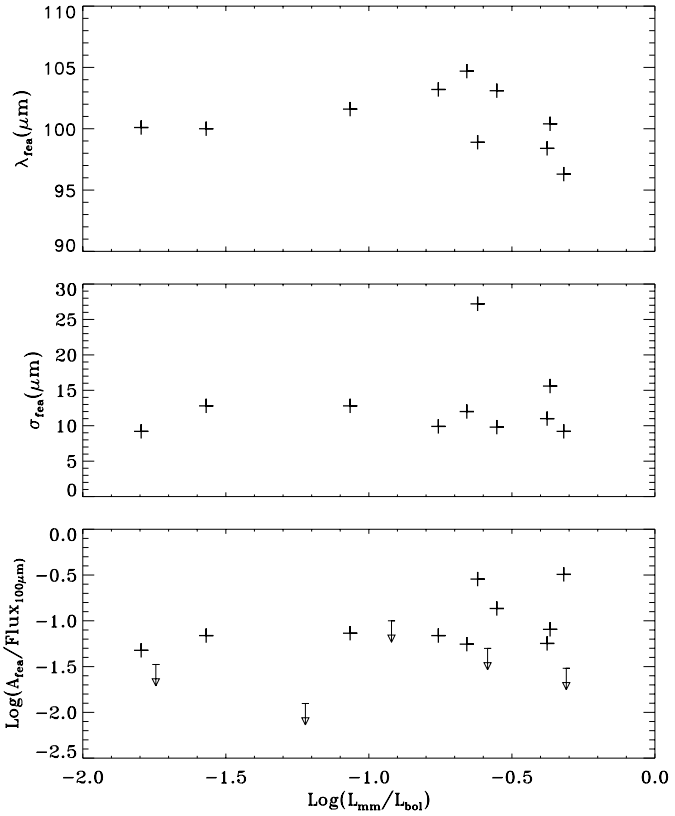

Fig. 11. The three parameters of the Gaussian fit versus the millimeter over the bolometric luminosity ratio, for the Class 0 sources sample.

carbonates with elements other than Ca, for example Mg or Fe, have features in the FIR too, but shifted significantly (e.g., tens of microns with respect to 100 μm; Farmer 1970). Hence, while varying amounts of impurities may be responsible for the shift in wavelength of the circumstellar feature, within this identification, the composition of the carbonate is by and large dominated by calcium. Of course, this identification awaits confirmation of other calcite feature in the spectra. Unfortunately, all the other three strong calcite features, around 7, 30 and 45 μm respectively, lie in difficult regions of the spectra. In particular, 45 μm marks the border between the LWS and SWS data, and, since the overlap between the two instruments is not very large, any detected and/or undetected feature at this wavelength are unreliable at the level of contrast to the expected continuum based on the longer wavelength band. In contrast, the 7 to 30 μm region – fully contained within the SWS range – is dominated by many features from several dust components (silicates, iron sulfide and PAHs) and ices (water, CO_2, NH_3, CH_4 and the so-called 6.8 μm band...), which severely hampers the study of calcite at these wavelengths. Again, the best example we have is EL29, whose SWS and LWS spectra have been analyzed in detail by Boogert et al. (2000, 2002), and we are unable to conclude anything based on those spectra. A careful analysis taking into account all the other identified dust and ice components is certainly worthwhile and it will be the subject of a dedicated future study.

Finally, hydrous silicates show a feature near 110 μm (Malfait et al. 1999; Bouwman et al. 2003). However, this feature is much broader than the 90–100 μm feature observed in these protostars and hence we consider it unlikely that this circumstellar feature is due to this mineral.

3.4. Calcite content

Following the hypothesis that the 90–110 μm feature is due to calcite, we have quantified the amount of calcite required to reproduce the observed feature in each source. To do this, we have determined the best fit of the LWS data compared to the calcite laboratory data, leaving the feature strength as the free parameter. Thus, we have assumed that the dust processing responsible for the peak shifts (e.g., inclusion of impurities) does not substantially influence the intrinsic strength of the feature. Figure 12 compares the LWS spectra of EL29 and L1448-mm respectively, with the best fit obtained with calcite. The result of the fits are reported in Table 1, where we present the mass of calcite for each source where the feature has been detected, as well as the ratio between the warm mass dust and the calcite. To estimate the warm dust mass, we adopted a mass absorption coefficient of $k_{60\,\mu m} = 4$ g^{-1} cm^2 (Ossenkopf & Henning 1994). This value is the average between the values obtained by Ossenkopf & Henning (1994) for grains with a thin and thick mantle respectively, and for a medium density of 10^6 cm^{-3}. The calcite over warm dust (e.g. silicates) mass ratio varies between 0.05% (in EL29) and almost 1% (extreme case HH24-MM), with an average value of 0.2%. For comparison, the ratio is 0.26% in NGC 6302, and 1% in NGC 1333-IRAS 4, the first sources where calcite was detected (Kemper et al. 2002a; Paper I).

Finally, Fig. 13 shows the histogram of the fraction of the elemental abundance of calcium (2×10^{-6}; Snow 1984) locked in the calcite and we conclude that, on average, about 10% to 30% of the calcium is locked in calcite. Hence, the formation mechanism of calcite must be relatively efficient.

4. Summary and conclusions

We have reported the analysis of LWS spectra of 32 protostars of low to intermediate mass. Most of them belong to one of two classes: Class 0 low mass sources and Herbig AeBe intermediate mass sources, respectively. We have found that more than half of the analyzed spectra present an excess feature in the 90–110 μm region.

The peak position of this feature is observed to vary from source to source. In Class 0 sources, the feature peaks at $\geq$96 μm , whereas in Herbig AeBe sources it peaks at shorter wavelengths. Correlations with properties of the sources, like luminosity and dust temperature, suggest that the peak position depends on the ("continuum") dust temperature but not on the source luminosity. Apparently, the characteristics of the dust carrier are sensitive to the dust temperature, the dust formation process, and/or the history of the dust.

We have presented arguments for the identification of the carrier of the feature with calcite. Reasonable fits to the observed feature are obtained with the laboratory measured spectrum of calcite, $CaCO_3$. The observed variations in peak

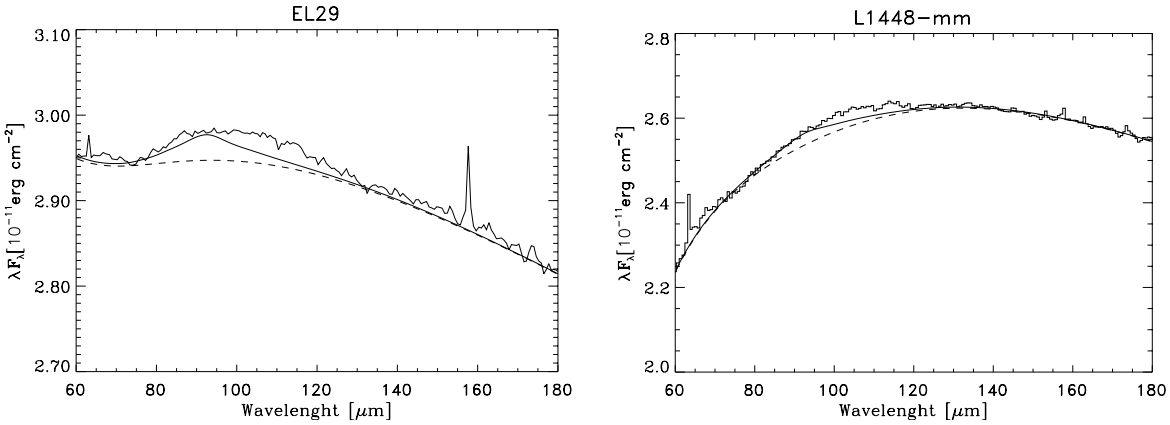

Fig. 12. *On the left*, the LWS observed spectrum of EL29 (thin line), compared with the 3-modified-blackbody best fit (dashed line), and the best fit obtained adding the calcite feature to the continuum (thick line). *Right panel* shows the same informations for L1448-mm.

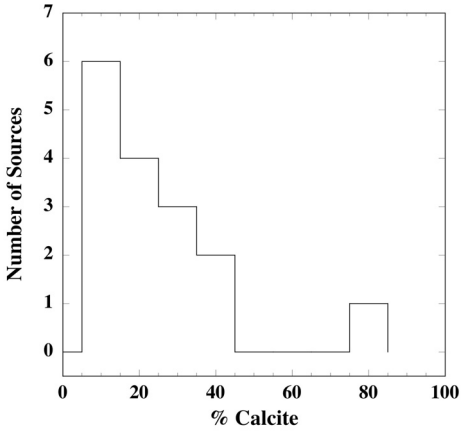

Fig. 13. Amount of calcium locked into calcite normalized to the elemental Calcium abundance.

position and width are attributed to the presence of traces of other cations (e.g., Mg, Fe) in the mineral.

As emphasized in previous studies on circumstellar calcite (Kemper et al. 2002a,b; Paper I), on the Earth calcite is formed via aqueous alteration. Likewise, the presence of calcite in IDPs and meteorites is attributed to aqueous alteration on the planetary body from which these collisional fragments were derived. However, the presence of carbonates in environments where liquid water is not expected, such as small dust grains in the circumstellar ejecta from stars in late stages of their evolution, points to other formation mechanisms. Several speculative pathways for the origin of carbonates in the absence of liquid water have been suggested, including direct condensation of carbonates from gaseous carbon dioxide and calcium oxide, interaction of accreted interstellar ice mantles with their underlying silicate cores over tens of thousands of years, and the formation of hydrated silicates through interaction of silicates with gaseous water followed by reaction with carbon dioxide to form carbonates (Kemper et al. 2002a). All of these proposed mechanisms suffer from a lack of relevant experimental support. Following Paper I, we emphasize that the presence of X-rays is one characteristic shared by both types of environments – hot planetary nebulae and young stellar objects – where circumstellar carbonates have been identified. Such X-rays may locally heat up accreted water ice and increase the H_2O mobility to a point similar to liquified water. While no X-ray studies are yet available for the Herbig AeBe stars in our sample, in general, Herbig AeBe stars are known to be strong X-ray emitter (Feigelson & Montmerle 1999). Likewise, Class I, II and III protostars are observed to be bright X-ray sources (Feigelson & Montmerle 1999). Class 0 sources are also suspected to harbor strong X-ray emitters at their center, but the observational confirmation is still missing because of the large absorbing column of their envelopes. A more detailed discussion of the calcite formation route is beyond the scope of this article. However, if X-rays are responsible for the increased mobility of H_2O molecules in ices, the same mechanism may also be involved in the formation of pre-biotic molecules[1].

Acknowledgements. We wish to thank C. Dominik for insightful discussions on the calcite identification and formation process, A. Boogert for providing us with the SWS spectrum of El29, E. Quirico and L.Wiesenfeld for elucidating the routes of formation of carbonates. We are also grateful to R. Gallino for comments on the manuscript. We thank the referee, C. Kemper, for a careful reading of the manuscript.

References

Allamandola, Tielens, & Barker 1989, ApJ, 733, 775
André, P., Ward-Thompson, D., & Barsony, M. 2000, Protostars & Planets IV
Boekel, R., Waters, L. B. F. M., Dominik, C., et al. 2003, A&A, L21
Boogert, A. C. A., Tielens, A. G. G. M., Ceccarelli, C., et al. 2000, A&A, 683, 698
Boogert, A. C. A., Hogerheijde, M. R., Ceccarelli, C., et al. 2002, A&A, 708, 723
Bottinelli, S., Ceccarelli, C., Lefloch, B., et al. 2004a, ApJ, 615, 354
Bottinelli, S., Ceccarelli, C., Neri, R., et al. 2004b, ApJ, 617, L69

[1] Indeed, several organic complex molecules – like methyl formate or methyl cyanide – have been found around at least two of the sources with the calcite feature: IRAS 16293-2422 (Cazaux et al. 2003; Bottinelli et al. 2004b) and NGC 1333-IRAS 4 (Bottinelli et al. 2004a).

Bouwman, J., de Koter, A., Dominik, C., & Waters, L. B. F. M. 2003, A&A, 401, 577
Bridges, J. C., Catling, D. C., Saxton, J. M., et al. 2001, Space Sci. Rev., 96, 365
Cazaux, S., Tielens, A. G. G. M., Ceccarelli, C., et al. 2003, ApJ, 593, L51
Ceccarelli, C., Loinard, L., Castets, A., Faure, A., & Lefloch, B. 2000, A&A, 362, 1122
Ceccarelli, C., Caux, E., Tielens, X., et al. 2002, A&A, 395, L29 (Paper I)
Draine, B. T. 2003, A&A, 1026-1037
Chandler, C. J., & Richer, J. S. 2000, ApJ, 530, 851
Clegg, P. E. C., Ade, P. A. R., Armand, C., et al. 1996, A&A, 315, L38
Feigelson, E. D., & Montmerle, T. 1999, ARA&A, 37, 363
Gooding, J. L., Wentworth, S. J., & Zolensky, M. E. 1988, Geochim. Cosmochim. Acta, 52, 909
Gooding, J. L., Wentworth, S. J., & Zolensky, M. E. 1991, Meteoritics, 26, 135
Henning, T., Begemann, B., Mutschke, H., & Dorschner, J. 1995, A&AS, 112, 143
Joergensen, J. K., Schoier, F. L., & van Dishoeck, E. F. 2002, A&A, 389, 908
Kemper, F., Jager, C., Waters, L. B. F. M., et al. 2002a, Nature, 415, 295 (KJW2002)
Kemper, F., Molster, F. J., Jager, C., & Waters, L. B. F. M. 2002b, A&A, 679, 690
Kessler, M. F., Steinz, J. A., Anderegg, M. E., et al. 1996, A&A, 315, L27
Koike, C., Hasegawa, H., & Hattori, T. 1982, Ap&SS, 88, 89
Malfait, K., Waelkens, C., Bouwman, J., De Koter, A., & Waters, L. B. F. M. 1999, A&A, 345, 181
Macdougall, J. D., Lugmair, G. W., & Kerridge, J. F. 1984, Nature, 307, 249
Maret, S., Ceccarelli, C., Caux, E., Tielens, A. G. G. M., & Castets, A. 2002, A&A, 573, 585
Onaka Takashi, & Okada Yoko 2003, ApJ, 872, 877
Ossenkopf, V., & Henning, T. 1994, A&A, 291, 943
Richardson, S. M. 1978, Metoritics, 13, 141
Snow, T. P. 1984, ApJ, 287, 238
Treiman, A. H. 1995, Metoritics, 30, 294
Wentworth, S. J., & Gooding, J. L. 1994, Metoritics, 29, 861